BAMS Article

# Saildrone

## Adaptively Sampling the Marine Environment

C. L. Gentemann, Joel P. Scott, Piero L. F. Mazzini, Cassia Pianca, Santha Akella, Peter J. Minnett, Peter Cornillon, Baylor Fox-Kemper, Ivona Cetinić, T. Mike Chin, Jose Gomez-Valdes, Jorge Vazquez-Cuervo, Vardis Tsontos, Lisan Yu, Richard Jenkins, Sebastien De Halleux, Dave Peacock, and Nora Cohen

**ABSTRACT:** From 11 April to 11 June 2018 a new type of ocean observing platform, the Saildrone surface vehicle, collected data on a round-trip, 60-day cruise from San Francisco Bay, down the U.S. and Mexican coast to Guadalupe Island. The cruise track was selected to optimize the science team's validation and science objectives. The validation objectives include establishing the accuracy of these new measurements. The scientific objectives include validation of satellite-derived fluxes, sea surface temperatures, and wind vectors and studies of upwelling dynamics, river plumes, air–sea interactions including frontal regions, and diurnal warming regions. On this deployment, the Saildrone carried 16 atmospheric and oceanographic sensors. Future planned cruises (with open data policies) are focused on improving our understanding of air–sea fluxes in the Arctic Ocean and around North Brazil Current rings.

https://doi.org/10.1175/BAMS-D-19-0015.1
Corresponding author: C. L. Gentemann, cgentemann@faralloninstitute.org
In final form 6 January 2020

**AFFILIATIONS: Gentemann**—Farallon Institute, Petaluma, California, and Earth and Space Research, Seattle, Washington; **Scott**—Science Applications International Corporation, NASA Goddard Space Flight Center, Greenbelt, Maryland; **Mazzini and Pianca**—Virginia Institute of Marine Science, William & Mary, Gloucester Point, Virginia; **Akella**—NASA Goddard Space Flight Center, Greenbelt, Maryland; **Minnett**—University of Miami, Miami, Florida; **Cornillon**—University of Rhode Island, Kingston, Rhode Island; **Fox-Kemper**—Brown University, Providence, Rhode Island; **Cetinić**—University Space Research Associates, NASA Goddard Space Flight Center, Greenbelt, Maryland; **Chin, Vazquez-Cuervo, and Tsontos**—Jet Propulsion Laboratory, California Institute of Technology, Pasadena, California; **Gomez-Valdes**—Ensenada Center for Scientific Research and Higher Education, Ensenada, Mexico; **Yu**—Woods Hole Oceanographic Institution, Woods Hole, Massachusetts; **Jenkins, De Halleux, Peacock, and Cohen**—Saildrone Inc., Alameda, California

The California coastal waters are important for the economy, society (this is the coast of the most populous state in the union), national security (they are the home waters of the Navy's Pacific fleet), and environment (it is along an eastern boundary current with biologically important upwelling). In the California Current region, the air–land–sea interface is complex, characterized by coastal promontories, upwelling jets and shadows, river plumes, and a narrow continental shelf that affects coastal dynamics producing highly variable sea surface temperature (SST) and concentration of the photosynthetic pigment chlorophyll a (Chl) (Checkley and Barth 2009; Strub and James 1995; Kelly et al. 1998; Brink et al. 2000). Along the U.S. and Mexican west coast, upwelling induces a flux of cold, nutrient-rich, dense, low-in-oxygen, and acidic waters to the surface ocean layers, leading to important air–sea and coastal–open ocean interactions (Sverdrup et al. 1942).

Due to its economic importance, the California Current System is one of the most studied and well-monitored upwelling systems in the world, including high-frequency (HF) radar for surface currents, regular oceanographic research cruises, and moored buoys for near-surface meteorological measurements and ocean temperature. Yet, even in this heavily sampled region, there are substantial gaps not filled by the current sampling strategy. Geostationary and polar-orbiting satellites provide discrete glimpses of the spatial structuring at the air–sea interface for a limited subset of environmental parameters. Temporal evolution of features can be provided by moored buoys but the fixed locations limit their use in understanding spatiotemporal structures and spatial scales of dynamical interactions. Other in situ platforms, such as subsurface gliders, floats, and drifters, provide valuable vertical and subsurface oceanographic measurements critical for measuring ocean heat content and transport, ocean velocities, thermohaline circulation, and other oceanographic applications. Wave Gliders provide both surface atmospheric (wind speed and direction, atmospheric pressure, and air temperature) and subsurface oceanographic observations and are able to travel at velocities of typically 0.8 m $s^{-1}$. The Saildrone measurements provide significant value to certain types of scientific studies through their design as a solar-powered, movable, steerable platform that samples a wide variety of air–sea-interface and upper-ocean parameters, especially in regions where it is difficult to deploy and maintain other types of assets. Wave Gliders and Saildrones both provide air–sea measurements that address the need for flexible, deployable, movable in situ observational assets, with each vehicle providing different capabilities for different types of scientific investigations. Wave Gliders can provide subsurface observations while Saildrones provide interfacial observations. The Saildrone vehicle's advantage is for science applications needing rapid spatial sampling (it can travel at up to 4 m $s^{-1}$), with additional atmospheric and oceanographic measurements needed to advance research into upwelling dynamics, submesoscale variability, and air–sea fluxes in the vicinity of ocean fronts, diurnal warming modeling, carbon cycling, and biophysical interactions and coupled atmosphere–ocean modeling and data assimilation. It is important to assess the accuracy of Saildrone observations for science.

We believe that such an assessment is important for two reasons: first, the Saildrone business model is different from the way research has been previously accomplished. Instead of purchasing equipment, which scientists then maintain, calibrate, and deploy, Saildrone owns and operates the vehicles and sensors, it is the data that are purchased. Second, there may be deployment issues associated with some of the instruments because of the nature of the vehicle. In the following we touch briefly on the former with a bit more discussion devoted to the latter.


**Fig. 1. The Saildrone vehicle returning to San Francisco on 11 Jun 2018. The wind anemometer is visible at the top of the wing and solar panels are on both the wing and the vehicle hull. Image credit: Saildrone/Gentemann.**

## Saildrone surface vehicles

Saildrone surface vehicles capture observations at the air–sea interface using autonomous technology, providing a dynamic method of capturing air–sea fluxes and other key ocean variables (Fig. 1). These vehicles combine wind-powered vehicle technology with solar-powered meteorological and oceanographic sensors for long-range data collecting missions (Fig. 2). A detailed description of the Saildrone development is given by Meinig et al. (2019). Each vehicle consists of a 7-m narrow hull, a 5-m-tall hard wing, and a keel with a 2.5-m draft, weighing approximately 750 kg, and travel at an average speed of 1.25 m $s^{-1}$.

The sensor payload on this cruise consisted of 16 science-grade sensors measuring atmospheric pressure, air temperature and humidity, wind speed and direction, ocean skin SST,

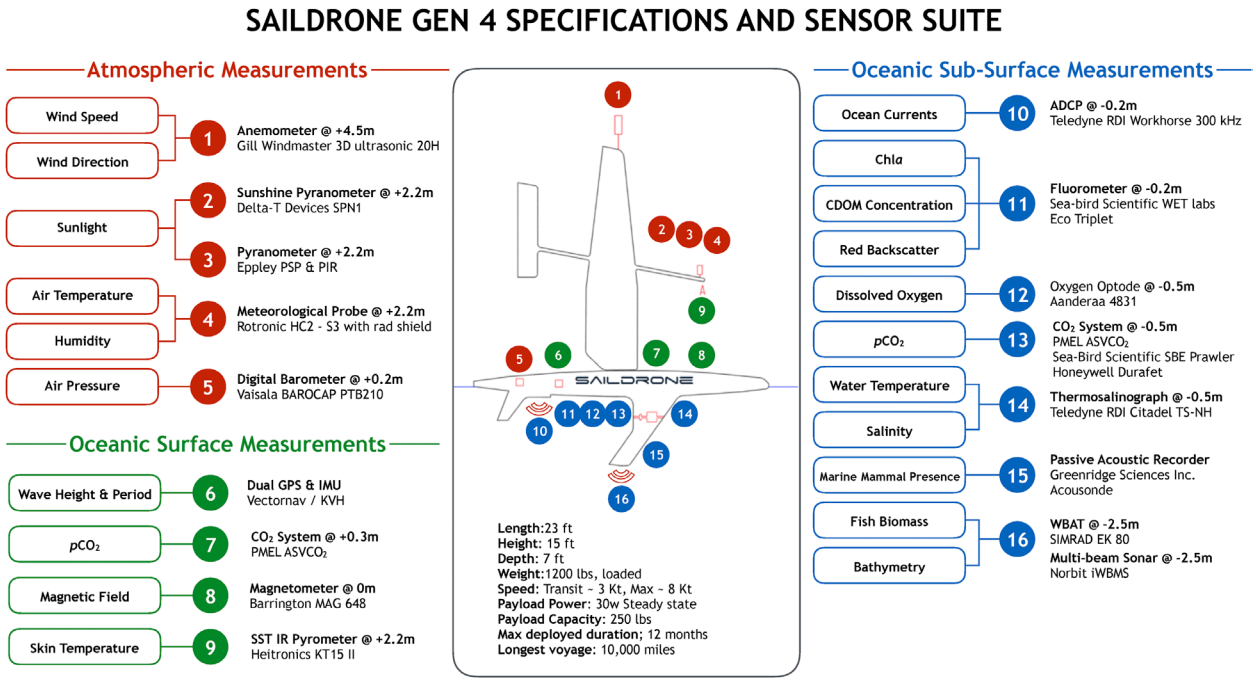


**Fig. 2. Instruments and their locations on the Saildrone generation 4 vehicle. Image credit: Saildrone.**

subsurface sea temperature, salinity, Chl fluorescence, colored dissolved organic matter (CDOM) fluorescence, red backscatter, dissolved oxygen, and upper-ocean 3D velocities (Table 1). Four SeaBird 56 (SBE 56) temperature loggers installed along the keel measured subsurface sea temperature at −0.295 to −1.785 m (Table 1). All sensors (except for the SBE 56) are connected to onboard computers and transmit data in real time via satellite connectivity, enabling adaptive sampling and real-time data analysis. Saildrones are under the supervision of a remote human pilot, but autonomously navigate from prescribed waypoint to waypoint, accounting for wind and currents, while staying within a user-defined corridor. To further ensure safe operation, each Saildrone is equipped with an automated identification system (AIS) transceiver (widely used in commercial shipping and private ocean sailing), navigation lights, radar reflector, high-visibility wing colors, and four onboard cameras.

All sensors carried by the Saildrone vehicle are initially calibrated by the sensor manufacturer and recalibrated according to the manufacturer's recommended timeline at their originating calibration facilities. Some sensors may also be recalibrated at an International Organization for Standardization/International Electrotechnical Commission (ISO/IEC) 17205 accredited calibration facility. Most sensors should not be affected by being mounted on a Saildrone vehicle versus another air–sea platform, with the following exceptions: sonic anemometer, ADCP, and flow-through measurements (e.g., CTD and dissolved oxygen). The Saildrone vehicle employs a three-axis sonic anemometer, mounted above the forward edge of the wing, collecting wind data during all sailing conditions. The forward edge of the wing is designed to cut through the wind and is (at its maximum) only 72 mm wide, and the wind measurement volume is 535 mm above the wing, and therefore should not contribute to flow distortion. The sonic anemometer and the ADCP are corrected for vehicle motion and orientation using highly accurate GPS-aided attitude and heading reference systems (AHRS) to generate samples that are corrected into an Earth reference frame independent of vehicle motion.

The flow-through sensors (CTD and oxygen), could be affected by vehicle temperatures at low flow-through velocities. This possible effect is unknown and cannot be corrected for a

**Table 1. Saildrone sensors.**

| Instrument | Observations | Sampling schedule | Height (m) |
|---|---|---|---|
| **Wing** | | | |
| Gill 1590-PK-020 | 3D wind direction, speed, and gust | 60 s on, 240 s off | 4.5 |
| Rotronic Hygroclip2 | Air temperature, relative humidity | 60 s on, 240 s off | 2.2 |
| Heitronics KT15.82.IIP | Skin SST | 30 s on, 270 s off | 2.2 |
| 4 × USB cams | Visible cameras | — | — |
| **Hull** | | | |
| Teledyne Citadel CTD-NH | Seawater temperature, seawater salinity, flow-through sensor | 12 s on, 48 s off | −0.6 |
| Aanderaa Oxygen Optode | Seawater oxygen fractional saturation, flow-through sensor | 10 s on, 50 s off | −0.6 |
| WET Laboratories Eco Triplet-w | Chlorophyll fluorescence, colored dissolved organic matter fluorescence, optical backscatter at 650 nm | 10 s on, 50 s off | −0.25 |
| Vaisala PTB 210 A1A1B | Air pressure | 60 s on, 240 s off | 0.2 |
| Teledyne Workhorse 300 kHz | 3D surface velocities | — | — |
| Seabird 56 | Seawater temperature | 2 s on, 2 s off | −0.295<br>−0.985<br>−1.420<br>−1.785 |

priori (or at least there is no a priori known correction, unlike the ADCP motion correction) and must be investigated using external data sources. We will explore this issue below in a validation of the CTD measurements from this cruise.

Several papers have previously explored the accuracy of the measurements collected aboard a Saildrone vehicle. First, the accuracy of Saildrone measurements were examined using nearby ship observations during a separate deployment, 1–10 May 2015 (Cokelet et al. 2015). The root-mean-square (RMS) wind speed difference was 0.62 m $s^{-1}$ and RMS wind direction difference of 3.8°. Saildrone subsurface sea temperatures had an RMS difference of 0.042°C and salinity measurements had an RMS difference of 0.01 practical salinity unit (PSU). Another validation of Saildrone measurements is from 18 October to 6 November 2017, when two Saildrone vehicles circled a Woods Hole Oceanographic Institution (WHOI) Salinity Processes in the Upper Ocean Regional Study 2 (SPURS-2) buoy that carried the Air–Sea Interaction Meteorology System (ASIMET), located in the tropical Pacific at 10°N, 125°W (Zhang et al. 2019). This analysis found the Saildrone versus ASIMET buoy RMS wind speed difference was 0.63 m $s^{-1}$, wind direction RMS difference of 16.0°, air temperature RMS difference of 0.31°C, relative humidity RMS difference of 2.3%, subsurface sea temperature RMS difference of 0.047°C, and salinity of 0.075 PSU. In this comparison, the wind speed RMS difference is higher than expected, but the authors point out that flow distortion around the Saildrone may be smaller than around the large WHOI buoy, and this may account for some of the difference. The RMS differences in wind direction are higher than expected, but smaller than the local variability and are adequate to resolve wind direction in this region. The subsurface sea temperature and salinity measurements show excellent agreement, for most comparisons.

These initial results are promising, but with only 10 (19) days of ship (buoy) collocations, in a limited range of environmental conditions, further validations of the Saildrone observations are necessary to assess the platform's accuracy under a wider range of environmental conditions.

## Cruise description

From 11 April to 11 June 2018, a Saildrone vehicle navigated round trip from San Francisco, southward to Guadalupe Island (Saildrone 2018). The route was designed to sample upwelling regions, diurnal warming events, frontal structures, and provide in situ buoy and glider collocation validation data (Fig. 3; Table 2). During the first half of the route, the Saildrone sailed, close to the coast, circling moored buoys, sailed over a glider track and near drifting buoys deployed by Centro de Investigación Científica y de Educación Superior de Ensenada (CICESE). The return leg was farther offshore and focused on sampling fronts. On the southward California coastal leg, the vehicle was primarily tasked from moored buoy to moored buoy, with a 100-km detour to sample across a glider track. Near Baja the vehicle was tasked to sample near drifting buoys deployed by CICESE, then tasked to continue southward sampling frontal regions near the coast. Data from the Baja deployment are available through the NASA

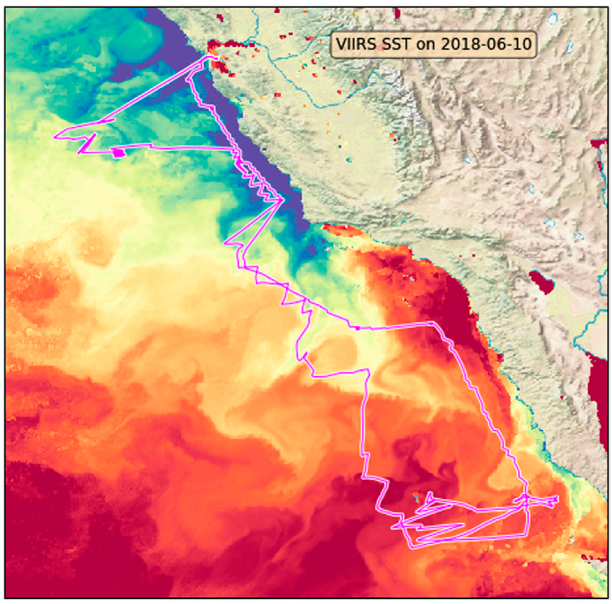


**Fig. 3. Cruise track for the 2018 Baja Saildrone cruise. VIIRS SSTs on 10 Jun 2018 are in the background. The prevalent wind direction was to the south, as seen by the relatively straight lines on the downward portion of the cruise, and the zig-zags (tacks) back-and-forth on the return leg.**

**Table 2. Timeline for Saildrone SD-1002, 11 Apr–11 Jun 2018 Baja cruise. Note that five-digit numbers herein are buoys identifiers.**

| Date | Description |
|---|---|
| 11 Apr | Depart SF, sail to buoy 46012 |
| 12 Apr | Arrive at 46012, circle 2 h, sail to 46042 |
| 12–13 Apr | Arrive 46042, circle 11 h, sail to 46028 |
| 14 Apr | Arrive 46028, circle 14 h, sail to 46011 |
| 15 Apr | Arrive 46011, circle 5 h, sail to SIO glider line |
| 16–17 Apr | Follow glider line to 46047 |
| 18–19 Apr | Arrive 46047, circle 11 h, sail to 46086 |
| 20 Apr | Arrive 46086, circle 14 h |
| 20–26 Apr | Sail along Baja coast to 28.428 094°, –116.114 588° to meet up with Lagrangian drifters |
| 27 Apr–16 May | Sail in region near Guadalupe Island with strong fronts and diurnal warming |
| 16–26 May | Sail northward to 46412 |
| 26–31 May | Arrive 46412, sail to 46011 |
| 31 May–1 Jun | Arrive 46011, circle 4 h, sail to 46028 |
| 1–3 Jun | Arrive 46028, circle 10 h, sail to 36.296 167°, –125.334 668°, where a strong front with a pinched-off eddy exists |
| 3–4 Jun | Cross-cut sampling of pinched-off eddy |
| 4–9 Jun | Along- and across-wind sampling of frontal feature |
| 9 Jun | Sail toward San Francisco Bay |
| 11 Jun | Vehicle recovery |

Physical Oceanography Distributed Active Archive Center (PO.DAAC).[1] Further information and resources are online (at https://podaac.jpl.nasa.gov/Saildrone). Data have also been incorporated into a free, open source, a software system for the analysis of large Earth observation datasets, Felyx.[2] For this paper, we will present a validation of the Saildrone observations and a few science highlights.

## Data

This cruise carried seven instruments for measuring sea temperature. Skin SST was measured by an Heitronics CT-10 infrared (IR) radiometer, subsurface SST, at –0.6 m, was measured by Teledyne Citadel CTD-NH and an Aanderaa Dissolved Oxygen instruments in a shared flow-through tube, and four SBE 56 temperature loggers were installed at different depths along the hull. Time series of the temperature data are shown in Fig. 4. During the cruise, there were four days (20 April and 14, 25, and 26 May) with upper-ocean thermal stratification (diurnal warming) where the observed temperatures diverged from each other. With those data points removed from the analysis, the accuracy of the different SST measurements was determined (Table 3) by comparison them to the deepest SBE 56. The three other SBE 56s had biases less than or equal to 0.003 K and standard deviations less than or equal to 0.08 K. The Teledyne (Aanderaa) –0.6-m SST measurements had a mean bias of 0.002 K (–0.014 K) and standard deviation of 0.04 K (0.04 K), which was lower than the comparisons with the SBE 56s. For days free of diurnal warming these results indicate that although –0.6-m SST measurements are taken via a flow-through passage, they are not being affected by the platform temperature. Platform heating could affect the flow-through observations during diurnal events when the flow-through velocities may be low. Figures 4b–d show the different temperature measurements during diurnal events, relative to the deepest observation at –1.785 m. The variability in temperature increases during diurnal events, but in all cases the shallowest (–0.295 m) measurement shows the largest

[1] https://doi.org/10.5067/SDRON-SURF0
[2] http://hrdds.ifremer.fr/

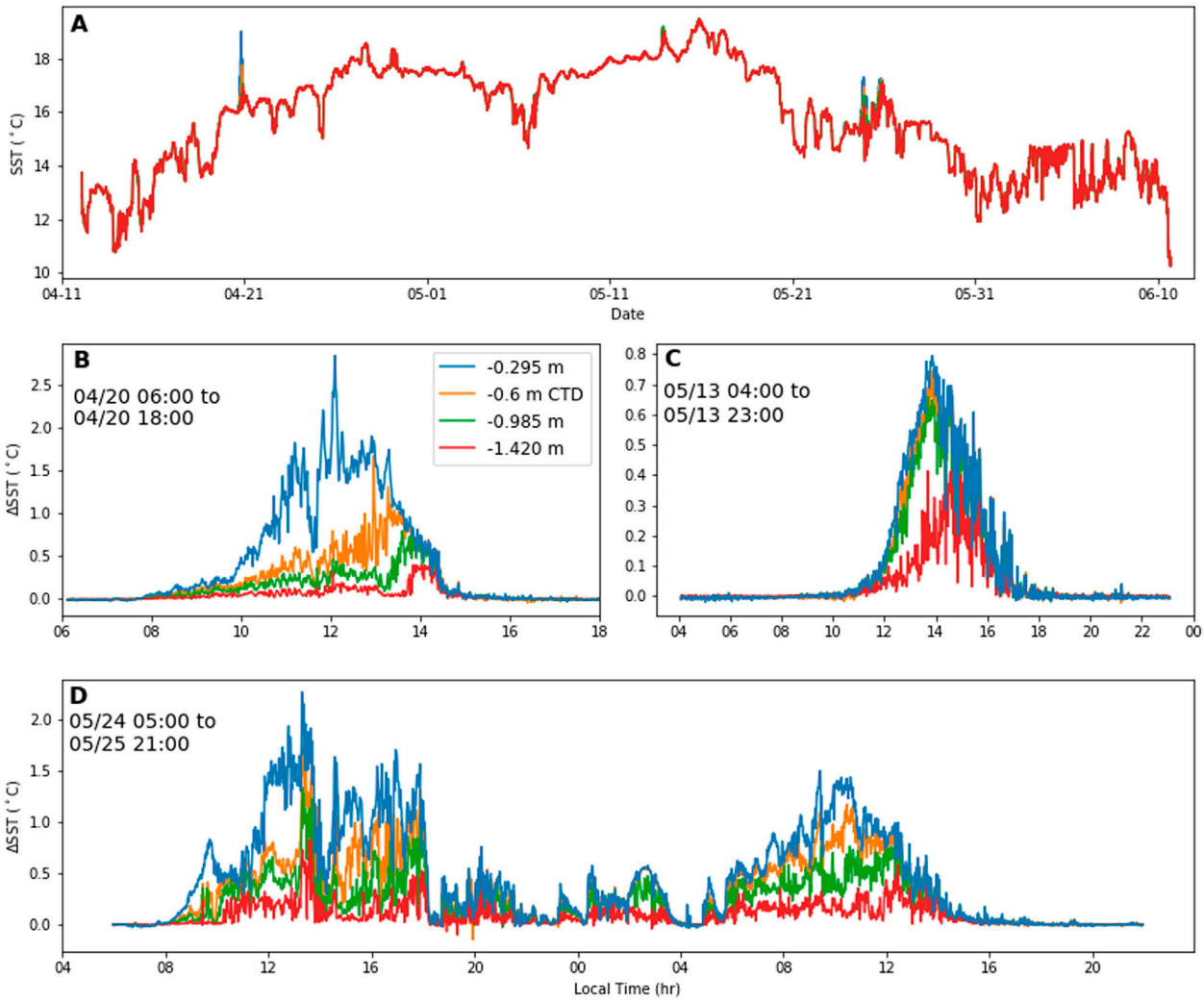


**Fig. 4. Time series of Saildrone ocean temperature measurements from CTD and the four SBE 56 temperature loggers. (a) The complete cruise time series. (b)– (d) The four days with diurnal warming. The color of the lines indicates the different measurement depths.**

**Table 3. Comparison of different Saildrone subsurface and skin SST measurements (K). The three days with diurnal warming were excluded from the comparisons. The Teledyne Citadel, Aanderaa Oxygen Optode, and Heitronics KT15 are designed as CTD, O2, and IR, respectively.**

| Depth and type of sensor differences | Mean bias | Median bias | Correlation | Standard deviation | Robust standard deviation | Mean average error | Number of measurements |
|---|---|---|---|---|---|---|---|
| $SBE_{-0.295} - SBE_{-1.785}$ | 0.003 | −0.004 | 1.00 | 0.076 | 0.004 | 0.01 | 77708 |
| $SBE_{-0.985} - SBE_{-1.785}$ | 0.002 | −0.003 | 1.00 | 0.065 | 0.003 | 0.01 | 77708 |
| $SBE_{-1.420} - SBE_{-1.785}$ | 0.001 | −0.002 | 1.00 | 0.054 | 0.002 | 0.01 | 77708 |
| $CTD_{-0.6} - SBE_{-1.785}$ | 0.002 | −0.001 | 1.00 | 0.042 | 0.004 | 0.01 | 77478 |
| $O2_{-0.6} - SBE_{-1.785}$ | −0.014 | −0.015 | 1.00 | 0.042 | 0.005 | 0.02 | 77478 |
| $IR - SBE_{-1.785}$ | −0.212 | −0.178 | 0.99 | 0.229 | 0.259 | 0.25 | 76997 |

amplitude of warming that decreases with increasing depth. As the warming decreases on each day, the two flow-through measurements at −0.6 m never exceed the shallower warming measured at −0.295 m. These results indicate that for the days that would most likely exhibit any platform heating effects on the flow-through temperature measurements, any effect appears to be within the expected geophysical and instrumental noise.

During the cruise, the Saildrone circled six moored buoys for short periods as a validation exercise (Table 4). These buoys carried a variety of sensor payloads, with different manufacturer stated accuracies. Here we provide overall statistics, with a more complete analysis and comparison of the different payloads in preparation. Saildrone 1-min data were averaged to match buoy data averages (10 min for winds, last 8 min of each hour for all other data). SST, air temperature, wind speed and direction show biases and standard deviations consistent with comparisons to other in situ observation platforms. There is a bias, –13.31 hPa, between the buoy and vehicle air pressure data across all buoys indicating a problem with the Saildrone sensor. Examination of the data indicates that this error appears to be a constant offset. While correctable for this cruise, this discrepancy was only discovered through comparison with ancillary data postcruise. A comparison of wind direction accuracy (Fig. 5a) shows an increase scatter below 3 m $s^{-1}$, between the direction measured by the Saildrone's sonic anemometer and the moored buoy's four-blade, impeller-driven, wind vane sensors. These low winds only occurred for buoy 46086, which Saildrone circled for approximately 12 h, which is not a substantial amount of data. Gilhousen (1987) compared collocated buoys that used wind vanes for speed and direction and also found an increased scatter at low winds, which

**Table 4. Saildrone matchup comparison summary. For the buoy data, only data within 5.5 km were used and the Saildrone data were averaged to match the buoy temporal averaging. The wind direction excludes collocations where the Saildrone wind speed were less than 3 m $s^{-1}$. Diurnal warming events were removed from the SST comparisons. Satellite matchups were within 3 h and 25 km. Hourly two-dimensional time-averaged model files were compared to the corresponding hourly averaged values from collocated Saildrone data. In coastal environments, Chl fluorescence has a non-Gaussian, lognormal distribution. Consequently, mean square error metrics are not suitable, and multiplicative mean bias and multiplicative MAE are reported instead (Seegers et al. 2018)**

| | | Mean bias | Median bias | Standard deviation | Robust standard deviation | Spearman's rank correlation | MAE | *N* |
|---|---|---|---|---|---|---|---|---|
| **SST (K)** | Buoy | –0.010 | –0.030 | 0.220 | 0.160 | 0.990 | 0.160 | 87 |
| | MUR | 0.320 | 0.290 | 0.410 | 0.340 | 0.980 | 0.400 | 5,833 |
| | AVHRR-OI | –0.030 | 0.050 | 0.590 | 0.652 | 0.950 | 0.603 | 60 |
| | MODIS-A | 0.123 | 0.156 | 0.314 | 0.190 | 0.990 | 0.271 | 20 |
| | MODIS-T | –0.008 | 0.343 | 0.896 | 0.155 | 0.930 | 0.215 | 40 |
| | VIIRS-SNPP | 0.131 | 0.065 | 0.255 | 0.146 | 0.990 | 0.202 | 31 |
| **SSS (PSU)** | SMAP | –0.160 | 0.212 | 0.330 | 0.248 | 0.610 | 0.756 | 60 |
| **Air temperature (K)** | Buoy | 0.010 | 0.000 | 0.170 | 0.120 | 0.980 | 0.130 | 87 |
| | GEOS-FP | –0.160 | –0.160 | 0.560 | 0.610 | 0.927 | 0.470 | 1,345 |
| | MERRA-2 | –0.040 | –0.030 | 0.590 | 0.620 | 0.918 | 0.450 | 1,345 |
| **Air pressure (hPa)** | Buoy | –13.310 | –16.120 | 6.290 | 0.340 | 0.610 | 13.470 | 87 |
| | GEOS-FP | –13.200 | –13.350 | 1.160 | 1.170 | 0.981 | 13.200 | 1,345 |
| | MERRA-2 | –12.940 | –13.180 | 1.690 | 1.370 | 0.798 | 12.940 | 1,345 |
| **Chl ($\mu$g $L^{-1}$)** | MODIS-A | 2.930 | 3.185 | — | — | — | 2.930 | 221 |
| | VIIRS-SNPP | 2.009 | 1.977 | — | — | — | 2.028 | 346 |
| **Wind speed (m $s^{-1}$)** | Buoy | 0.320 | 0.300 | 0.520 | 0.540 | 0.980 | 0.490 | 307 |
| | CCMP V2 | 0.090 | –0.020 | 1.050 | 0.850 | 0.900 | 0.760 | 492 |
| | GEOS-FP | 1.267 | 1.339 | 1.274 | 1.38 | 0.874 | 1.524 | 1,345 |
| | MERRA-2 | 1.149 | 1.084 | 1.742 | 1.891 | 0.727 | 1.646 | 1,345 |
| **Wind direction (°)** | Buoy | –6.260 | –6.590 | 5.770 | 5.320 | 0.950 | 7.080 | 278 |
| | CCMP V2 | –3.440 | –3.060 | 14.030 | 6.390 | 0.580 | 7.780 | 492 |
| | GEOS-FP | –7.754 | –5.106 | 38.405 | 9.822 | 0.359 | 13.672 | 1,345 |
| | MERRA-2 | –11.194 | –8.384 | 45.530 | 14.421 | 0.180 | 19.448 | 1,345 |

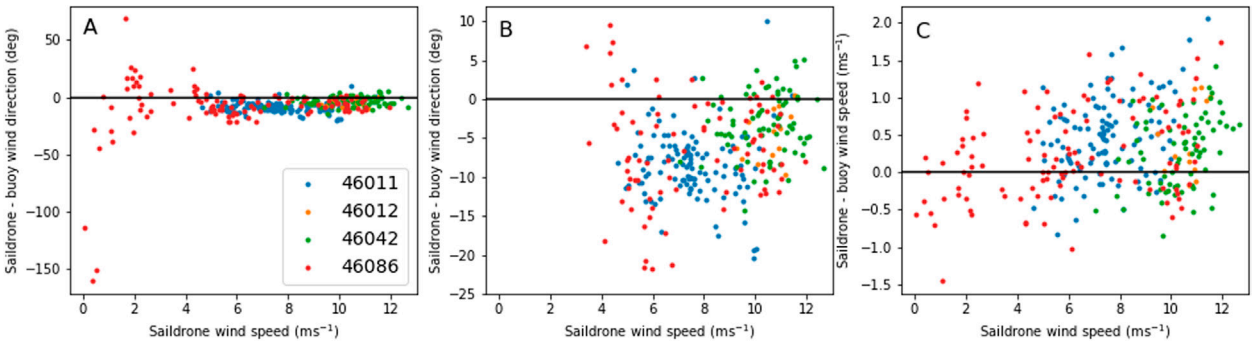


**Fig. 5. Saildrone minus buoy differences in (a) wind direction, (b) wind direction, and (c) wind speed as a function of wind speed. At low wind speeds, the scatter increases and this only occurred at buoy 46086. Note that (b) is as in (a), but with wind speeds less than 3 m $s^{-1}$ removed.**

he attributed to an increase in variability at low winds. Bowen (2005) compared a wind vane and sonic anemometer during a 1-yr deployment in a low-wind location and found increased scatter below 2 m $s^{-1}$. He proposed the scatter might be due to "inadequate" wind vane response at low wind speeds. This increased variability is concerning because buoy wind direction data are used by virtually every weather and ocean numerical prediction model and unreliable wind direction data can impact model accuracy. Figures 5b and 5c show comparisons between Saildrone and buoy wind speeds (direction), showing no clear dependence on wind speed. While these initial results are promising, a longer buoy validation cruise involving multiple buoys and Saildrone vehicles would be desirable in the future to develop a more robust understanding of Saildrone vehicle accuracy for measuring wind speed and direction.

***Data summary.*** Saildrone measurements of SST, air temperature, air pressure, salinity, Chl, and wind vectors were validated using collocated in situ moored buoy measurements and showed reasonable agreement compared to satellite observations and model analyses (Table 4). The results here are in general agreement with the results from Zhang et al. (2019), but showed some differences that are likely related to the different environmental conditions sampled. For wind speed (direction) bias was similar (higher) but the STD was larger (smaller) than the SPURS collocations, likely due to the higher wind speeds measured during this cruise. The different results in these studies underscore the need for longer Saildrone buoy collocation efforts. The satellite and model comparisons revealed differences between individual products that require further investigation and underscore the value of Saildrone measurements for satellite retrieval algorithm and model development.

***Data quality issues.*** Data quality issues were identified through comparisons between similar sensors carried on the Saildrone and in situ buoy collocations. First, the air pressure sensor appears to have malfunctioned with a constant bias of ~–13 hPa for the entire cruise (Table 2). This was easily identified from the in situ buoy collocations. It is suspected that moisture infiltrated the instrument during a previous deployment leading to early failure. For future deployments, the barometer on Saildrones will be housed in an additional waterproof box, with careful venting of the sensing port. To minimize recurrence of this failure, it is now standard procedure for Saildrone Inc. to complete two instrument precruise evaluations, first, to a reference device at the Saildrone Inc. headquarters in San Francisco Bay, then a second, short cruise alongside other vehicles in the same mission, after deployment at the launch site.

The second data quality issue is related to the measurement of the ocean skin temperature using a single downward-looking infrared radiometer. The sea surface is not a perfect blackbody, radiation is both absorbed and reflected, so viewing the surface with a passive

radiometer will yield an observation that contains both radiation emitted from and reflected by the sea surface (Hanafin and Minnett 2005). The Saildrone skin temperature measurement for this cruise was found to have large errors due to the lack of a correction for reflected sky radiation. An IR skin radiometer skin SST measurement should naturally be about −0.17 K cooler than a subsurface temperature measurement because of the skin effect (Donlon et al. 2002; Minnett et al. 2011). While Table 3 shows a mean bias of −0.21 K, which is not too far off the expected value of −0.17 K, a probability density function of the bias distribution shows two distinct peaks, one at −0.54 K and another at −0.06 K. This result was investigated further using satellite imagery. A time series of the Saildrone skin SST minus the SBE 56 show consistent differences, jumping between the two peaks depending on cloudy and clear-sky conditions. The sky condition was further confirmed through onboard imagery from Saildrone cameras. At this time, the Saildrone skin SST from this deployment is not recommended for applications that require biases of less than 0.5 K.

Saildrone is currently testing an upward-looking radiometer that could be used to correct for the reflected sky radiation, but measurements from that radiometer remain of unknown accuracy. Skin radiometer measurements from a Saildrone are challenging because of the necessary correction for the contribution of reflected sky radiation and it remains to be seen if this is possible at an accuracy useful for science. Current skin temperature measurements are only available using expensive, specialized, instrumentation deployed on a relatively small number of ships. If future Saildrone vehicles are able to accurately measure skin temperature, it would be an important technological advancement. Additional information on this type of measurement is presented in Donlon et al. (2014).

***Use of Saildrone data for satellite validation and algorithm development.*** Traditional pointwise approaches to validating remotely sensed satellite retrievals are inadequate in regions where mesoscale and submesoscale spatial variability dominate the coastal dynamics, such as the California Current (Castro et al. 2018). Satellite validation data are conventionally obtained from moored and drifting buoys, research vessels, and ships of opportunity, but these sources are often limited to specific geographic regions. Additionally, satellite retrievals of sea surface salinity (SSS) and Chl are difficult to validate since methods of data collection (either through in situ instrumentation of collection of discrete samples) are expensive and challenging to deploy and collect. Therefore, Saildrone measurements may serve as a valuable source of satellite validation and algorithm development data in certain regions, once the accuracy of the Saildrone instruments have been assessed.

Saildrone measurements were compared to remotely sensed data from a variety of sources throughout the 60-day deployment (Fig. 6, Table 4) and show general agreement with satellite retrievals. Saildrone measurements diverging wildly from satellite retrievals of SST, SSS, bio-optical parameters, and wind speed would be concerning, but this is not the observed case. However, the Saildrone measurements do not identically

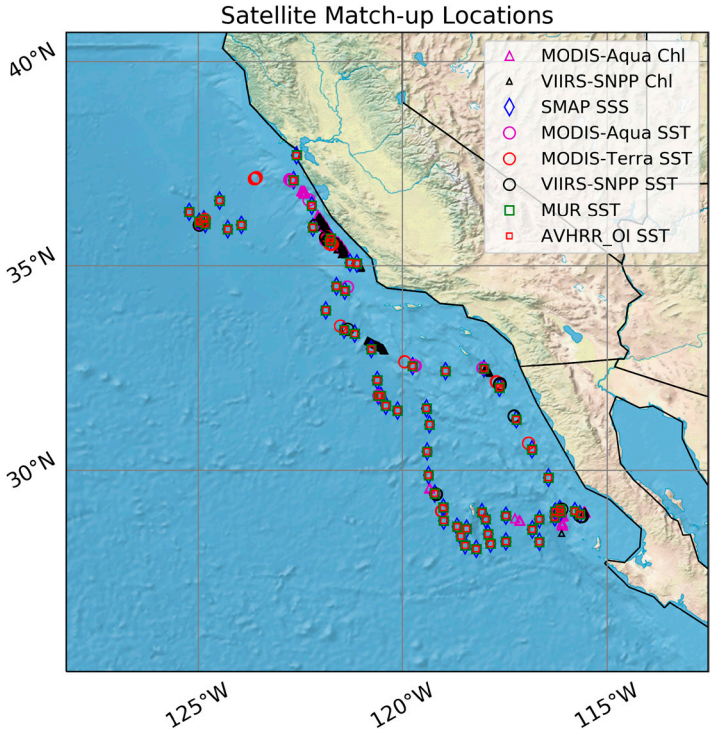


**Fig. 6. Saildrone matchup locations with satellite-based products.**

agree with satellite retrievals at all times, and it is in these cases that we can learn about certain features (i.e., subpixel variability, frontal features, biological processes, etc.) that are often not accounted for in remote sensing algorithms, but that the Saildrone is capable of observing.

Satellite retrievals of SST show general agreement with the Saildrone observations, as evidenced by similar performance metrics arising when satellite SST retrievals are compared to conventional validation data sources, presented by Minnett et al. (2019), accounting for the expected differences between surface and subsurface measurements. One notable exception is the MUR SSTs that show a larger bias (0.32 K) than other SST analyses. This is likely due to a transient bias present in one of the satellite SST used by the MUR analysis system. A more detailed analysis of satellite SST and SSS comparisons is presented in Vazquez-Cuervo et al. (2019). Comparisons with SST indicated excellent agreement with overall biases approaching zero. Meissner et al. (2019) also show the utility of Saildrone in assessing reprocessing efforts of remote sensing data, especially in coastal areas. Decreased biases were clearly seen in the reprocessed data. Saildrone Chl fluorescence show large biases relative to the satellite Chl retrievals due to the lack of coincident, discrete Chl measurements to further constrain the Chl to Chl fluorescence ratio beyond the manufacturer's calibration (Roesler et al. 2017), and due to the effects of non-photochemical quenching (NPQ), which occurs during periods of high solar insolation.[3] Further validation results and analysis of bio-optical Saildrone observations may be found in Scott et al. (2020).

The preliminary comparisons of satellite retrievals to Saildrone SST, SSS, and ocean vector winds (OVWs) in Table 4 demonstrate future viability of Saildrones for research applications in complex and remote regions of the world's oceans and as a future validation source for satellite-derived SSTs. Saildrone measurements in data scarce regions will have great value for satellite algorithm development and validation purposes.

***Potential for model improvements.*** Measurements near the air–sea interface are essential to improve models and to use as constraints in data assimilation systems, such as the Goddard Earth Observing System weather analysis and prediction (referred to as GEOS-FP)[4] and MERRA-2 (Gelaro et al. 2017) system.[5] Overall, there is good agreement between modeled winds and Saildrone measurements (Table 4). The hourly variability in eastward wind is better resolved than the northward wind, with the higher-resolution GEOS-FP model outperforming the lower-resolution MERRA-2 model. A detailed comparison, including time series of Saildrone measurements of winds, air temperature, air pressure, and near-surface water temperatures with GEOS-FP and MERRA-2 is given in Akella and Gentemann (2019, hereafter AG2019). The robustness of these global data assimilation systems is evident from a comparison of the air pressure (Fig. 6 of AG2019), which also shows that both the GEOS-FP and MERRA-2 have about 15-hPa-higher pressure than the Saildrone measured data (as described in previous section, a sensor calibration problem). Diurnal warming events (described above) are also in agreement with GEOS-FP (Fig. 9 of AG2019). The Saildrone data provide two different ways to improve models. First, assimilation of the Saildrone data would be of value in data sparse regions (after development of suitable quality control procedures), and second, differences in model and observed values are valuable clues for improving modeled dynamics through process studies. Since the Saildrone can measure data across the air–sea interface (in data-sparse regions), it can provide valuable data, otherwise not available from traditional observing systems. Such collocated data are extremely useful in identifying biases in general circulation models and data assimilation systems (e.g., AG2019).

[3] NPQ is correctable via the relationship between particulate backscatter (bbp) and Chl fluorescence (Xing et al. 2018; Zhang et al. 2009), but has not yet been performed for this cruise.

[4] Data URL: https://gmao.gsfc.nasa.gov/GMAO_products/NRT_products.php

[5] Data URL: https://gmao.gsfc.nasa.gov/reanalysis/MERRA-2/

## Science applications

***River plume fronts.*** This Saildrone cruise provided an excellent opportunity to survey the San Francisco Bay plume (SFBP), acquiring high-resolution information of this poorly surveyed plume, while allowing us to test the capability of this new sampling platform for future studies of freshwater fronts in coastal regions. River plumes are the primary link between riverine–estuarine and oceanic environments, they influence continental shelf circulation and mixing, and deliver substances and materials to the coastal ocean, including sediments, nutrients, pollutants (Chant 2011; Horner-Devine et al. 2015). Plumes from small and midsized estuaries have typical spatial scales $O(1–10)$ km, while time scales of variability can be as short as a few hours, presenting an observational challenge.

The Saildrone crossed the SFBP twice, first in the beginning of the cruise (11 April 2018) when daily averaged freshwater discharge[6] was relatively high, 2,350 $m^3 s^{-1}$, over one standard deviation above the monthly mean, and second, during the end of the cruise (11 June 2018), when spring runoff decreased and the discharge had fallen by an order of magnitude, to 190 $m^3 s^{-1}$, but within one standard deviation from the monthly mean. A sharp front, ~1 km wide, with a salinity change over 4 PSU, was located 6 km offshore from the mouth of the bay (Fig. 7). This distance is less than the length of the M2 tidal excursion from the Golden Gate, estimated to be 15 km (Cheng and Gartner 1984), suggesting that this distinct front separates the tidally modulated plume, or near field, from the plume midfield, where variability is dominated by subtidal time scales. In the plume near field, a 3-km-wide salinity peak was observed at 2.5 km offshore, with a 2–2.5-PSU salinity anomaly. This disruption from an offshore monotonic salinity increase points to a deviation from a simple radially spreading tidal plume, suggesting a more complex lateral circulation structure, similarly reported in other systems, such as the Columbia River plume (e.g., Horner-Devine et al. 2009; Kilcher and Nash 2010; Akan et al. 2018). Surface currents from HF radar show an along-coast southward jet crossing the Saildrone transect, which might explain the salinity peak due to lateral advection of higher-salinity shelf waters. The plume midfield did not present a simple linear offshore increase in salinity either with the nearly continuous high-resolution Saildrone survey showing salinity structure rich in small-scale features with a decorrelation scale estimated at 3 km. These small-scale structures reveal the complexity and spatial variability of the plume's circulation and mixing. Properly understanding plume structure is crucial for predicting its evolution and the delivery of the river-borne nutrients to the coastal ocean.

[6] Calculated from the "net delta outflow index" obtained from the California Department of Water Resources (https://water.ca.gov/).

CDOM exhibited an inverse relationship with salinity, as expected, with a significant correlation coefficient of −0.99. This relationship between CDOM and salinity in the SFBP confirms that optical characteristics of water may be used as a

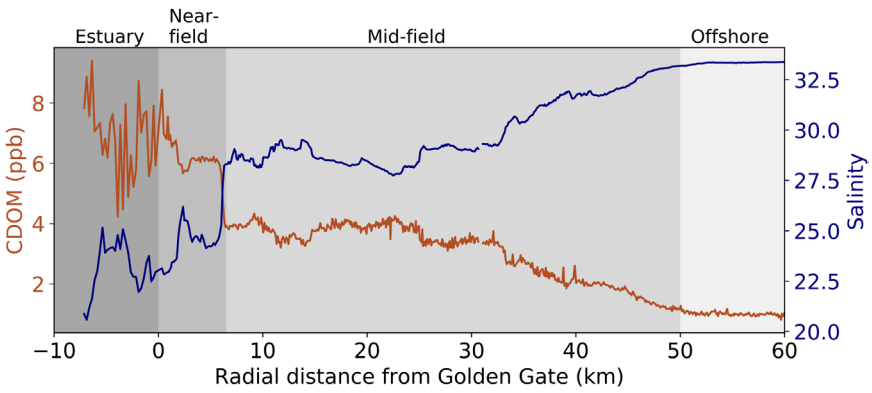


**Fig. 7. Near-surface salinity and colored dissolved organic matter (CDOM) as a function of radial distance from the Golden Gate Bridge (positive westward) obtained by the Saildrone on 11–12 April 2018. The Saildrone crossed San Francisco Bay mouth during the ebb tide when surface currents exiting the bay exceeded 1 m $s^{-1}$. The average velocity of the Saildrone during this transect was approximately 2 m $s^{-1}$, which demonstrates its suitability for surveying strong tidally modulated regions. Salinity ranged from 23 PSU just outside the mouth to 33.3 PSU offshore, varying over 10 PSU within the region influenced by the freshwater outflow. This region extended to 50 km offshore, occupying nearly the entire continental shelf in the Gulf of the Farallones.**

proxy to trace river plumes (e.g., Dzwonkowski and Yan 2005; Nezlin et al. 2005; Thomas and Weatherbee 2006; da Silva and Castelao 2018). These results encourage future studies pairing remotely sensed ocean color with autonomous platform data from Saildrone, providing synoptic measurements capable of resolving plumes with extensive surface areas. These measurements will allow us to address how plumes are impacted simultaneously by time variable wind forcing and river discharge, tides, and how they interact with complex topography.

***Upper-ocean diurnal warming.*** The upper-ocean temperature profile depends on the surface heat and momentum flux, subsurface absorption of solar radiation, and horizontal and vertical mixing (Soloviev and Lukas 2006; Fairall et al. 1996). The diurnal warming of the ocean surface from solar radiation is an important contribution to the subdaily variability in air–sea fluxes and affects both satellite SST algorithm development and validation (Donlon et al. 2002; Kawai and Wada 2007). Research into upper-ocean variability is critical to understanding surface forcing (i.e., fluxes, momentum, etc.), which affect subsurface temperatures that compose the seasonal cycle and are eventually mixed into the deeper ocean (Weller and Anderson 1996; Clayson and Bogdanoff 2013). Upper-ocean diurnal warming studies have been previously conducted via satellite surface observations, in situ subsurface measurements, and surface-based skin SST and upper-ocean temperature profile data from research vessels (Kawai and Wada 2007).

Passive microwave satellites measure SST and contemporaneous wind speed, yet these instruments are in high-inclination polar orbits only observing a location once or twice per day. Satellite observations in low-inclination orbits that cycle through the diurnal cycle are adequate for understanding the mean statistical shape and variability of diurnal warming at the surface, but not for assessing the temporal evolution or the vertical structure. Geostationary satellite SSTs are capable of measuring the temporal evolution of diurnal warming, but lack simultaneous wind speed observations needed to understand the effects of stratification and the ocean's response to momentum-induced mixing. In situ subsurface measurements from drifting or moored buoys provide hourly, or better, observations of SST. But most moored buoys, while measuring wind speed, lack information on diurnal upper-ocean stratification and have limited spatial coverage; whereas drifting buoys sample the global ocean but lack meteorological observations. There are a limited number of moored research buoys (e.g., WHOI, OceanSITES) that provide information on upper-ocean stratification and have improved instruments and temporal sampling.

Saildrones instrumented with additional temperature loggers, Table 1, minimizes these observational complications by providing data on surface and subsurface evolution of upper-ocean diurnal warming, while simultaneously observing the ancillary meteorological parameters necessary to develop advanced models of diurnal warming. The warming event (yellow and orange regions) differs from the surface temperatures of the nighttime satellite pass immediately following, seen in Fig. 8 by 0.5–1 K, shows the value of outfitting Saildrones with additional temperature loggers, which have proven to be highly accurate (Table 3). Periods when these along-keel SBE 56 loggers diverge from each other, highlight diurnal warming events, when the upper ocean becomes thermally stratified as a result of strong solar insolation and little near-surface mixing due to low wind speeds. The diurnal warming of almost 2 K in the top 1.5 m of the ocean, is most strongly concentrated at the surface and deepens through the day (Figs. 9a,b). Using the deepest keel temperature as a baseline will yield an accurate measurement of the diurnal stratification at shallower depths, provided warming does not extend further than the deepest keel temperature. Otherwise, an underestimate of the warming may result. Saildrone is currently exploring adding a temperature profiler to address this issue, but it currently is not part of the standard instrument suite. Observations of diurnal stratification with coincident atmospheric observations are scarce, but provide excellent

data for understanding diurnal warming and furthering model development (e.g., AG2019).

***Upper-ocean 3D currents.*** The diurnal warming event on 20 April 2018 shows the magnitude of the horizontal current and their components in the upper 80 m of the water column (Figs. 9c–e). During the first part of this period [2200 local solar time (LST) 19 April to 0700 LST 20 April; the vertical green line in each panel] the Saildrone was sailing around buoy 46086 and the time series is close to Eulerian—"close" in the sense that the observations are not at a fixed location but are very close to being so because the Saildrone is sailing in relatively tight circles around the mooring. As the vessel sailed away from the buoy the wind speed dropped to less than 2 m $s^{-1}$ and the speed of the Saildrone dropped to ~0.2 m $s^{-1}$ (again close to Eulerian) before increasing to >1 m $s^{-1}$ at ~1300 LST. The structure of the horizontal currents during these periods is intriguing.

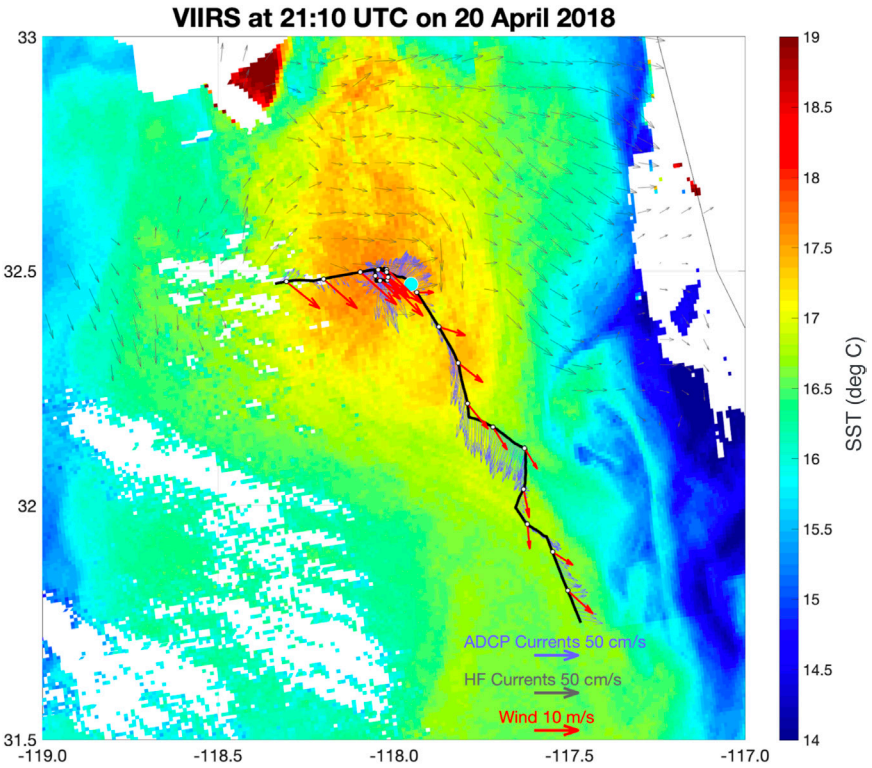


**Fig. 8. A diurnal warming event (large yellow-orange region) on 20 Apr 2018 with the Saildrone track (heavy black line), small white dots every 10 km along the track, and the location of the Saildrone at the time of the satellite image (cyan dot at 32.47°N, 117.95°W). Light blue vectors along the track show the uppermost ADCP currents (4.2 m). Red vectors show wind measured by the Saildrone. Gray vectors shows HF radar currents at 2100:00 UTC 20 Apr 2018. White indicates clouds or land. The square to the west of the cyan dot corresponds to the track of the Saildrone as it circumnavigated NOAA buoy 46086 five times providing a 14-h time series of near-surface temperature. Given that edges of the box were approximately 4 km long, the data collected during this period provide a Eulerian view (to within 3 km) of the surface properties measured by the Saildrone.**

From 2200 LST 19 April to 0400 20 April there is a distinct 5-m-thick minimum in the speed of the current at depths ranging from 20 to 30 m. Based on glider cruises in the region during the same period and the relative homogeneity of the velocities above these depths, we believe they correspond to the base of the mixed layer and will refer to them as such in the following. The depth of this layer shoals from 30 to 20 m with what appears to be an upward-propagating internal wave—the band of enhanced currents (Figs. 9d,e), which impinges on the bottom of the mixed layer. [The rotation of the current as it propagates upward is also clearly seen in videos of the current at different depths (not shown here).] Beneath the local minimum in the magnitude of the current, a layer of relatively higher horizontal speeds, ranging in thickness from 5 to 25 m, is evident from 2200 LST 19 April to 0900 LST 20 April, the time at which diurnal warming begins (Fig. 9b). During the diurnal warming event, 1000–1400 LST, the horizontal current increases uniformly throughout the mixed layer, but then decreases abruptly in the mixed layer to <10 cm $s^{-1}$ as the surface cools, while the current at the base of the mixed layer increases dramatically in a 10-m-thick layer to more than 35 cm $s^{-1}$. The layer of enhanced current at the bottom of the mixed layer remains intact until sunset (1900 LST) at which time it dissipates. The current throughout the mixed layer increases again later in the afternoon in conjunction with a temperature increase at the surface following a local minimum around

1600 LST. Both times that the surface temperature began to increase, the current also increased uniformly through the entire mixed layer. There were several other days with diurnal warm layers, but a uniform concomitant increase in the current is not seen in the mixed layer.

To further complicate the environment, upward-propagating internal waves beneath the mixed layer are also present. The rotational period of the currents in these waves is ~19 h, compared with the period of inertial oscillations, which is 21 h with currents rotating clockwise in the horizontal plane. These waves appear to be separated by ~13 h; although, this is difficult to see in Figs. 9d and 9e. The Saildrone data along with satellite-derived SST and HF radar currents reveal the complex interactions of the circulation in this region.

The role of diurnal warming and horizontal gradients play in these coastal dynamics is not clear presently, but the data raise a number of intriguing science questions. For example, does the increased kinetic energy in the mixed layer, which appears to be associated with diurnal warming, move to the bottom of the mixed layer following the warming event? Or, are we seeing a thermal wind adjustment of the mixed layer associated with changes in the horizontal density? Another possibility is that the increased current is associated with a reflection of an internal wave at the bottom of the mixed layer. And what gives rise to the thin layer of reduced current, again at the bottom of the mixed layer seen in the early part of the period? These questions highlight the value additional Saildrone deployments and HF radar current data to further study and understand coastal and diurnal events like these.

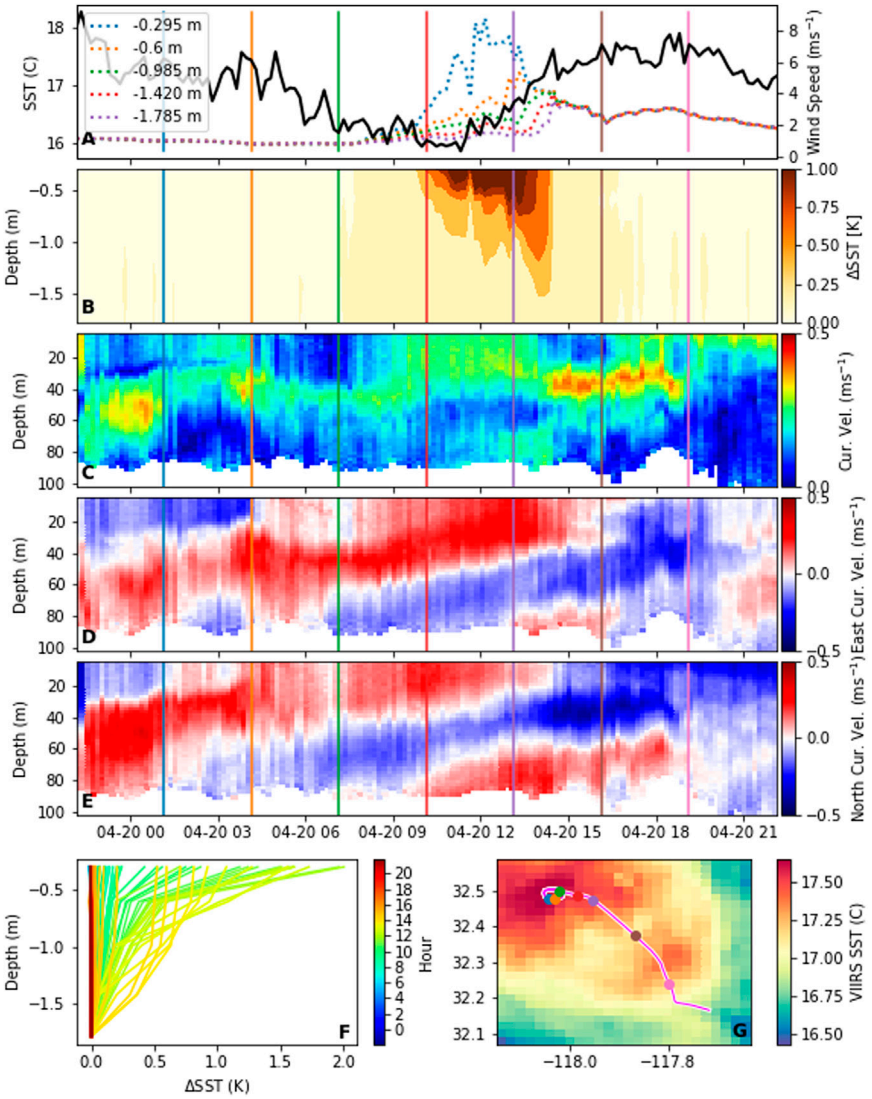


**Fig. 9. Diurnal warming on 20 Apr 2018, with local time shown in hours. (a) Diurnal warming stratification in the upper-ocean temperatures measured at different depths (dashed lines) and wind speed (black line). (b) Vertical temperature distribution of temperature. (c)–(e) Horizontal, eastward, and northward current velocities from the ADCP, respectively. (f) Another view of the evolution of warming with depth. (g) VIIRS SSTs in the region of sampling with the dots corresponding to the colored lines on all previous panels.**

***Heat fluxes along SST gradients.*** Enhanced SST spatial gradients (or fronts) with a magnitude of 0.2°–1°C (10 km)$^{-1}$ are frequently featured in Saildrone data. These SST fronts are a manifestation of the California Current System as a region of active frontogenesis (Castelao et al. 2006), and also highlight the influence of submesoscale and mesoscale SST variability on the atmosphere (e.g., Skyllingstad et al. 2007; Wenegrat and Arthur 2018; Renault et al.

2018; Thomas and Lee 2005; Shao et al. 2019). The SST gradients across a front give rise to spatial variations in buoyant stability of the marine atmospheric boundary layer, which modify surface turbulent heat fluxes and wind stress (Guymer et al. 1983; Businger and Shaw 1984; Small et al. 2008). The changes in ocean surface forcing, through mixing and energy transfer, allow coupling between the atmosphere and ocean to exist at frontal scales. Saildrones are well instrumented to study the frontal-scale air–sea interaction because of their coherent sampling of meteorological and oceanographic conditions and have the flexibility to sail along and through SST fronts, dynamically. On 18–19 April 2018 (Fig. 10) the Saildrone sampled fronts where the wind direction was both perpendicular and parallel to a strong oceanic front, defined by a sharp change in sea surface temperature. The data show the effects of wind direction, relative to an SST front, on the air–sea energy fluxes

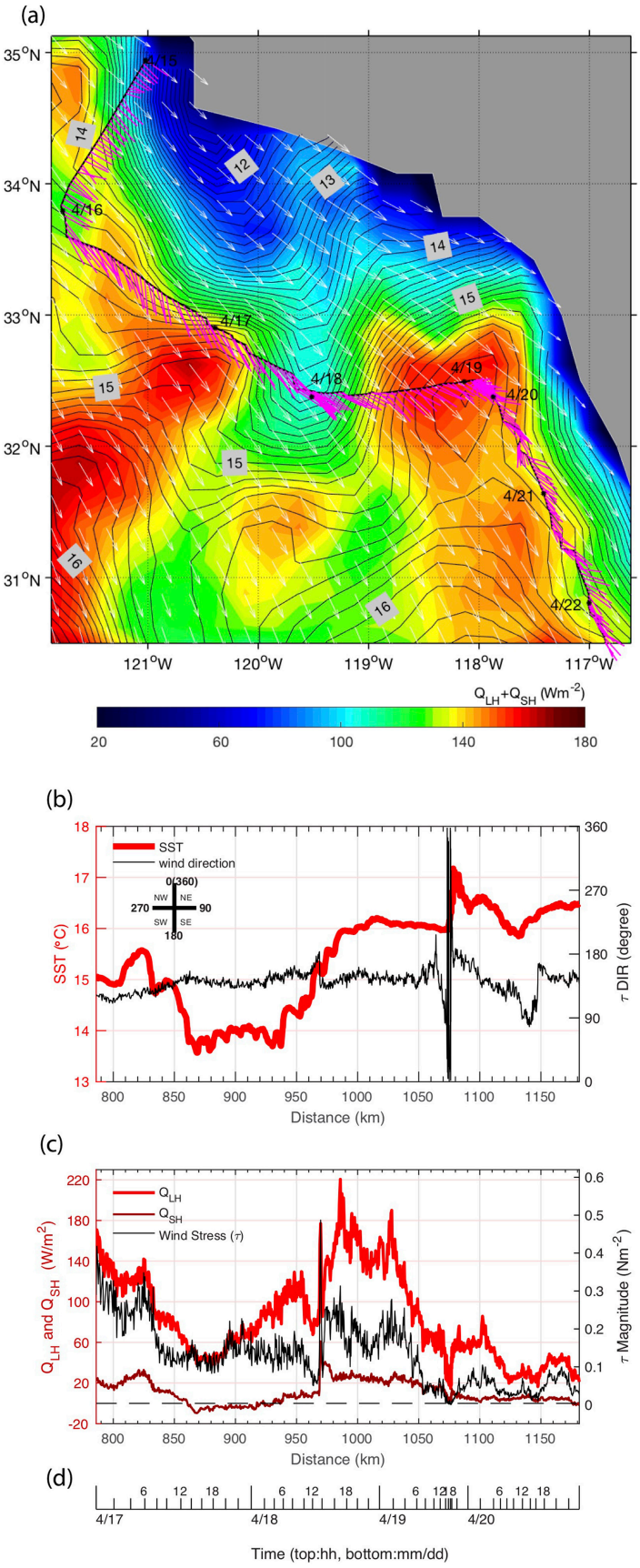


**Fig. 10. Variability of air–sea fluxes associated with two SST fronts. (a) Daily mean field of SST (black contours; interval: 0.1°C), wind stress $\tau$ (white vectors), and QLH + QSH (colors) on 18 April superimposed with the Saildrone's track and measurements of wind vectors (magenta). Saildrone surface fluxes ($\tau$, QLH, QSH) are based on COARE bulk flux algorithm, version 3.5 (Fairall et al. 2003) and produced by the high-resolution analysis of the Objectively Analyzed Air–Sea Fluxes (OAFlux) project (Yu 2019). (b) Time series of Saildrone measurements of SST (red) and wind stress direction (black) during 17–20 Apr (see the time mark placed at the bottom) (corresponding to the distance between 780 and 1,180 km that is marked on the *x* axis). (c) Time series of wind stress (black) and surface latent (QLH; red), and sensible (QSH; dark red) heat fluxes based on Saildrone measurements and COARE algorithm. (d) The *x* axis labeled by the measurement time with hours marked on the top and dates (month/day) on the bottom. The first front on 18 April, featuring a 2°C increase of SST in 12 h (over a distance of 500 km) from 0600 LST (940 km) to 1800 LST (990 km). Within the next 6 h, wind stress almost tripled from below 0.1 to 0.3 N m$^{-2}$, QLH increased by about 160 W m$^{-2}$, and QSH increased by about 20 W m$^{-2}$. The second front on 19 April, showing a 1°C sharp increase of SST within 1–2 h over a distance of 10 km (1,070–1,080 km). This front only incurred about a 60 W m$^{-2}$ increase in QLH, an 8 W m$^{-2}$ increase in QSH, and a less than 0.05 N m$^{-2}$ increase in winds, which account for about one-third of the changes induced by the first SST front. Wind directions were approximately perpendicular to the SST gradients during the first front, but nearly parallel with the SST isotherms during the second front. Surface wind stress $\tau$ and turbulent latent (QLH) and sensible (QSH) heat fluxes showed vastly different responses to the two SST fronts, because of the differences in relative direction of wind to SST gradients.**

associated with the front. Submesoscale theory has sought to describe such relationships (e.g., Thomas and Lee 2005; Suzuki et al. 2016), but the directionality has not been accounted for in large-scale model parameterizations or for global observational products, indicating an opportunity for these Saildrone measurements to reduce potential systematic biases in these systems.

## Future directions

During this 2-month cruise, Saildrones collected a new dataset with substantial scientific value. All instruments, except two, worked well and demonstrated encouraging accuracy, as compared to external data sources. Comparisons to satellite data and model analyses highlight the value of Saildrone measurements for future algorithm and numerical model improvements, especially in complex and data sparse oceanic regions. Results from four initial scientific studies demonstrated the utility of Saildrone platforms to conduct science and improve our understanding of the Earth system.

Saildrones are currently deployed around the world. In June 2019 alone, there were three circumnavigating Antarctica, six in the U.S. Arctic (four funded by NOAA and two by NASA), seven surveying fish stock off of the U.S. West Coast, four surveying the tropical Pacific, two surveying fish stock in Norway, and one conducting a multibeam bathymetry survey in the Gulf of Mexico. In 2020, Saildrone Inc. has deployed fleets in Europe, the Arctic, the tropical Pacific, the North American west coast, the Gulf of Mexico, the Atlantic, the Caribbean, and Antarctica. All NASA-funded Saildrone data are distributed openly and publicly from the NASA PO.DAAC. Saildrone Inc. is also openly distributing data from the Second Saildrone Award, in which the University of Rhode Island surveyed the Gulf Stream in the Atlantic during the Northern Hemisphere winter. In the next few years, the amount of data collected by these new platforms could have a substantial impact on our understanding of upper-ocean dynamics and the complex interactions between the ocean and atmosphere.

**Acknowledgments.** The Saildrone data collection mission was sponsored by the Saildrone Award, an annual data collection mission awarded by Saildrone Inc., and the Schmidt Family Foundation. The research was funded by the NASA Physical Oceanography Program Grant 80NSSC18K0837 and 80NSSC18K1441. The work by T. M. Chin, J. Vazquez-Cuerzo, and V. Tsontos was carried out at the Jet Propulsion Laboratory (JPL), California Institute of Technology, under a contract with the National Aeronautics and Space Administration (NASA). Piero L.F. Mazzini was supported by California Sea Grant Award NA18OAR4170073. We thank CeNCOOS for providing the HF radar data in the Gulf of the Farallones. Jose Gomez-Valdes was supported by CONACYT Grant 257125, and by CICESE. Work by Joel Scott and Ivona Cetinic was supported through NASA PACE. The work by Lisan Yu was supported by NOAA Ocean Observing and Monitoring Division under Grant NA14OAR4320158.

## References


Akan, Ç., J. C. McWilliams, S. Moghimi, and H. T. Özkan-Haller, 2018: Frontal dynamics at the edge of the Columbia River plume. *Ocean Modell.*, **122**, 1–12, https://doi.org/10.1016/j.ocemod.2017.12.001.

Akella, S. and C. Gentemann, 2019: GMAO research brief: Saildrone Baja field campaign: A comparison of surface meteorology with GEOS products. NASA Rep. GSFC-E-DAA-TN71693, 15 pp.

Blough, N. V., and R. del Vecchio, 2002: Chromophoric DOM in the coastal environment. *Biogeochemistry of Marine Dissolved Organic Matter*, D. A. Hansell and C. A. Carlson, Eds., Academic Press, 509–546.

Bowen, B. M., 2005: Improved wind and turbulence measurements using low cost 3-D sonic anemometers at a low wind site. *13th Symp. on Meteorological Observations and Instrumentation*, Savannah, GA, Amer. Meteor. Soc., 7.4., https://ams.confex.com/ams/15AppClimate/techprogram/paper_91957.htm.

Brink, K. H., R. C. Beardsley, J. Paduan, R. Limeburner, M. Caruso, and J. G. Sires, 2000: A view of the 1993–1994 California Current based on surface drifters, floats, and remotely sensed data. J. Geophys. Res.: Oceans, **105**, 8575–8604, https://doi.org/10.1029/1999JC900327.

Businger, J. A., and W. J. Shaw, 1984: The response of the marine boundary layer to mesoscale variations in sea-surface temperature. *Dyn. Atmos. Oceans*, **8**, 267–281, https://doi.org/10.1016/0377-0265(84)90012-5.

Castelao, R. M., T. P. Mavor, J. A. Barth, and L. C. Breaker, 2006: Sea surface temperature fronts in the California Current System from geostationary satellite observations. *J. Geophys. Res.*, **111**, C09026, https://doi.org/10.1029/2006JC003541.

Castro, S. L., L. A. Monzon, G. A. Wick, R. D. Lewis, and G. Beylkin, 2018: Subpixel variability and quality assessment of satellite sea surface temperature data using a novel high resolution multistage spectral interpolation (HRMSI) technique. *Remote Sens. Environ.*, **217**, 292–308, https://doi.org/10.1016/j.rse.2018.08.019.

Chant, R., 2011: Interactions between estuaries and coasts: River plumes their formation, transport, and dispersal. *Treatise on Estuarine and Coastal Science*, E. Wolanski and D. McLusky, Eds., Academic Press, 213–235.

Checkley, D. M., Jr., and J. A. Barth, 2009: Patterns and processes in the California Current System. *Prog. Oceanogr.*, **83**, 49–64, https://doi.org/10.1016/j.pocean.2009.07.028.

Cheng, R. T., and J. W. Gartner, 1984: Tides, tidal and residual currents in San Francisco Bay, California—Results of measurements 1979–1980. U.S. Geological Survey Water Resources Investigations Rep. 84-4339, 1737 pp.

Clayson, C. A., and A. S. Bogdanoff, 2013: The Effect of Diurnal Sea Surface Temperature Warming on Climatological Air–Sea Fluxes. J. Climate, **26**, 2546–2556, https://doi.org/10.1175/JCLI-D-12-00062.1.

Cokelet, E. D., C. Meinig, N. Lawrence-Slavas, P. J. Stabeno, C. W. Mordy, H. M. Tabisola, R. Jenkins, and J. N. Cross, 2015: The use of Saildrones to examine spring conditions in the Bering Sea. *OCEANS 2015*, Washington, DC, IEEE, https://doi.org/10.23919/OCEANS.2015.7404348.

da Silva, C. E., and R. M. Castelao, 2018: Mississippi River plume variability in the Gulf of Mexico from SMAP and MODIS-Aqua observations. *J. Geophys. Res. Oceans*, **123**, 6620–6638, https://doi.org/10.1029/2018JC014159.

Donlon, C. J., P. J. Minnett, C. L. Gentemann, T. J. Nightingale, I. J. Barton, B. Ward, and M. J. Murray, 2002: Toward improved validation of satellite sea surface skin temperature measurements for climate research. *J. Climate*, **15**, 353–369, https://doi.org/10.1175/1520-0442(2002)015<0353:TIVOSS>2.0.CO;2.

——, and Coauthors, 2014: Ship-borne thermal infrared radiometer systems. *Experimental Methods in the Physical Sciences*, G. Zibordi, C. J. Donlon, and A. C. Parr, Eds., Optical Radiometry for Ocean Climate Measurements, Vol. 47, Academic Press, 1079–4042.

Dzwonkowski, B., and X. Yan, 2005: Tracking of a Chesapeake Bay estuarine outflow plume with satellite-based ocean color data. *Cont. Shelf Res.*, **25**, 1942–1958, https://doi.org/10.1016/j.csr.2005.06.011.

Fairall, C. W., G. S. Young, E. F. Bradley, D. P. Rogers, and J. B. Edson, 1996: Bulk parameterization of air-sea fluxes for Tropical Ocean-Global Atmosphere Coupled-Ocean Atmosphere Response Experiment. *J. Geophys. Res.*, **101**, 3747–3764, https://doi.org/10.1029/95JC03205.

——, E. F. Bradley, J. E. Hare, A. A. Grachev, and J. B. Edson, 2003: Bulk parameterization of air–sea fluxes: Updates and verification for the COARE algorithm. *J. Climate*, **16**, 571–591, https://doi.org/10.1175/1520-0442(2003)016<0571:BPOASF>2.0.CO;2.

Gelaro, R., and Coauthors, 2017: The Modern-Era Retrospective Analysis for Research and Applications, version 2 (MERRA-2). *J. Climate*, **30**, 5419–5454, https://doi.org/10.1175/JCLI-D-16-0758.1.

Gilhousen, D. B., 1987: A field evaluation of NBDC moored buoy winds. *J. Atmos. Oceanic Technol.*, **4**, 94–104, https://doi.org/10.1175/1520-0426(1987)004<0094:AFEONM>2.0.CO;2.

Guymer, T. H., J. A. Businger, K. B. Katsaros, W. J. Shaw, P. K. Taylor, W. G. Large, and R. E. Payne, 1983: Transfer processes at the air-sea interface. *Philos. Trans. Roy. Soc. London*, **308A**, 253–273, https://doi.org/10.1098/RSTA.1983.0003.

Hanafin, J. A., and P. J. Minnett, 2005: Measurements of the infrared emissivity of a wind-roughened sea surface. *Appl. Opt.*, **44**, 398–411, https://doi.org/10.1364/AO.44.000398.

Horner-Devine, A. R., D. A. Jay, P. M. Orton, and E. Y. Spahn, 2009: A conceptual model of the strongly tidal Columbia River plume. *J. Mar. Syst.*, **78**, 460–475, https://doi.org/10.1016/j.jmarsys.2008.11.025.

——, R. D. Hetland, and D. G. MacDonald, 2015: Mixing and transport in coastal river plumes. *Annu. Rev. Fluid Mech.*, **47**, 569–594, https://doi.org/10.1146/annurev-fluid-010313-141408.

Kawai, Y., and A. Wada, 2007: Diurnal sea surface temperature variation and its impact on the atmosphere and ocean: A review. *J. Oceanogr.*, **63**, 721–744, https://doi.org/10.1007/s10872-007-0063-0.

Kelly, K. A., R. C. Beardsley, R. Limeburner, K. H. Brink, J. D. Paduan, and T. K. Chereskin, 1998: Variability of the near-surface eddy kinetic energy in the California Current based on altimetric, drifter, and moored current data. *J. Geophys. Res.*, **103**, 13 067–13 083, https://doi.org/10.1029/97JC03760.

Kilcher, L. F., and J. D. Nash, 2010: Structure and dynamics of the Columbia River tidal plume front. *J. Geophys. Res.*, **115**, C05S90, https://doi.org/10.1029/2009JC006066.

Meinig, C., and Coauthors, 2019: Public–private partnerships to advance regional ocean-observing capabilities: A Saildrone and NOAA-PMEL case study and future considerations to expand to global scale observing. *Front. Mar. Sci.*, **6**, 448, https://doi.org/10.3389/fmars.2019.00448.

Meissner, T., F. Wentz, A. Manaster, and R. Lindsley, 2019: NASA/RSS SMAP salinity: Version 4.0 validated release. Remote Sensing Systems Tech. Rep. 082219, 55 pp.

Minnett, P. J., M. Smith, and B. Ward, 2011: Measurements of the oceanic thermal skin effect. *Deep-Sea Res. II*, **58**, 861–868, https://doi.org/10.1016/j.dsr2.2010.10.024.

——, and Coauthors, 2019: Half a century of satellite remote sensing of sea-surface temperature. *Remote Sens. Environ.*, **233**, 111366, https://doi.org/10.1016/j.rse.2019.111366.

Nezlin, N. P., P. M. DiGiacomo, E. D. Stein, and D. Ackerman, 2005: Stormwater runoff plumes observed by SeaWiFS radiometer in the Southern California Bight. *Remote Sens. Environ.*, **98**, 494–510, https://doi.org/10.1016/j.rse.2005.08.008.

Renault, L., J. C. McWilliams, and J. Gula, 2018: Dampening of submesoscale currents by air-sea stress coupling in the Californian upwelling system. *Sci. Rep.*, **8**, 13388, https://doi.org/10.1038/s41598-018-31602-3.

Roesler, C., and Coauthors, 2017: Recommendations for obtaining unbiased chlorophyll estimates from in situ chlorophyll fluorometers: A global analysis of WET Labs ECO sensors. *Limnol. Oceanogr. Methods*, **15**, 572–585, https://doi.org/10.1002/lom3.10185.

Saildrone, 2018: Saildrone Baja field campaign surface and ADCP measurements, version 1.0. PO.DAAC, accessed 2 January 2019, http://doi.org/10.5067/SDRON-SURF0.

Scott, J., S. Crooke, I. Cetinic, C. E. Del Castillo, and C. Gentemann, 2020: Correcting non-photochemical quenching of Saildrone chlorophyll-a fluorescence for evaluation of satellite ocean color retrievals. *Opt. Express*, **28**, 4274–4285, https://doi.org/10.1364/OE.382029.

Seegers, B. N., R. P. Stumpf, B. A. Schaeffer, K. A. Loftin, and P. J. Werdell, 2018: Performance metrics for the assessment of satellite data products: An ocean color case study. *Opt. Express*, **26**, 7404–7422, https://doi.org/10.1364/OE.26.007404.

Shao, M., and Coauthors, 2019: The variability of winds and fluxes observed near submesoscale fronts. *J. Geophys. Res. Oceans*, **124**, 7756–7780, https://doi.org/10.1029/2019JC015236.

Skyllingstad, E. D., D. Vickers, L. Mahrt, and R. Samelson, 2007: Effects of mesoscale sea-surface temperature fronts on the marine atmospheric boundary layer. *Bound.-Layer Meteor.*, **123**, 219–237, https://doi.org/10.1007/s10546-006-9127-8.

Small, R. J., and Coauthors, 2008: Air–sea interaction over ocean fronts and eddies. *Dyn. Atmos. Oceans*, **45**, 274–319, https://doi.org/10.1016/j.dynatmoce.2008.01.001.

Soloviev, A., and R. Lukas, 2006: *The Near-Surface Layer of the Ocean: Structure, Dynamics and Applications*. Springer, 574 pp.

Strub, P. T., and C. James, 1995: The large-scale summer circulation of the California Current. *Geophys. Res. Lett.*, **22**, 207–210, https://doi.org/10.1029/94GL03011.

Suzuki, N., B. Fox-Kemper, P. E. Hamlington, and L. P. Van Roekel, 2016: Surface waves affect frontogenesis. *J. Geophys. Res. Oceans*, **121**, 3597–3624, https://doi.org/10.1002/2015JC011563.

Sverdrup, H. U., M. W. Johnson, and R. H. Fleming, 1942: *The Oceans: Their Physics, Chemistry, and General Biology*. Prentice-Hall, 1087 pp.

Thomas, A. C., and R. A. Weatherbee, 2006: Satellite-measured temporal variability of the Columbia River plume. *Remote Sens. Environ.*, **100**, 167–178, https://doi.org/10.1016/j.rse.2005.10.018.

Thomas, L. N., and C. M. Lee, 2005: Intensification of ocean fronts by down-front winds. *J. Phys. Oceanogr.*, **35**, 1086–1102, https://doi.org/10.1175/JPO2737.1.

Vazquez-Cuervo, J. S., J. Gomez-Valdes, M. Bouali, L. E. Miranda, T. Van der Stocken, W. Tang, and C. Gentemann, 2019: Using Saildrones to validate satellite-derived sea surface salinity and sea surface temperature along the California/Baja coast. *Remote Sens.*, **11**, 1964, https://doi.org/10.3390/rs11171964.

Weller, R. A., and S. P. Anderson, 1996: Surface meteorology and air–sea fluxes in the western equatorial Pacific warm pool during the TOGA Coupled Ocean–Atmosphere Response Experiment. *J. Climate*, **9**, 1959–1990, https://doi.org/10.1175/1520-0442(1996)009<1959:SMAASF>2.0.CO;2.

Wenegrat, J. O., and R. S. Arthur, 2018: Response of the atmospheric boundary layer to sub-mesoscale sea surface temperature fronts. *Geophys. Res. Lett.*, **45**, 13 505–13 512, https://doi.org/10.1029/2018GL081034.

Xing, X., N. Briggs, E. Boss, and H. Claustre, 2018: Improved correction for non-photochemical quenching of in situ chlorophyll fluorescence based on a synchronous irradiance profile. *Opt. Express*, **26**, 24734, https://doi.org/10.1364/OE.26.024734.

Yu, L., 2019: Global air–sea fluxes of heat, fresh water, and momentum: Energy budget closure and unanswered questions. *Annu. Rev. Mar. Sci.*, **11**, 227–248, https://doi.org/10.1146/annurev-marine-010816-060704.

Zhang, D., and Coauthors, 2019: Comparing air-sea flux measurements from a new unmanned surface vehicle and proven platforms during the SPURS-2 field campaign. *Oceanography*, **32** (2), 122–133, https://doi.org/10.5670/OCEANOG.2019.220.

Zhang, X., L. Hu, and M. X. He, 2009: Scattering by pure seawater: Effect of salinity. *Opt. Express*, **17**, 5698–5710, https://doi.org/10.1364/OE.17.005698.